Scott–Russel Linkage-Based Triboelectric Self-Powered Sensor for Contact Material-Independent Force Sensing and Tactile Recognition

*Dongwon Seo, Jimin Kong, and Jihoon Chung**

The rapid growth of Internet of Things (IoT) in recent years has increased demand for various sensors to collect a wide range of data. Among various sensors, the demand for force sensors that can recognize physical phenomena in 3D space has notably increased. Recent research has focused on developing energy harvesting methods for sensors to address their maintenance problems. Triboelectric nanogenerator (TENG) based force sensors are a promising solution for converting external motion into electrical signals. However, conventional TENG-based force sensors that use the signal peak can negatively affect data accuracy. In this study, a Scott–Russell linkage-inspired TENG (SRI-TENG) is developed. The SRI-TENG has completely separate signal generation and measurement sections, and the number of peaks in the electrical output is measured to prevent disturbing output signals. In addition, the lubricant liquid enhances durability, enabling stable force signal measurements for 270 000 cycles. The SRI system demonstrates consistent peak counts and high accuracy across different contacting surfaces, indicating that it can function as a contact material-independent self-powered force sensor. Furthermore, using a deep learning method, it is demonstrated that it can function as a multimodal sensor by realizing the tactile properties of various materials.
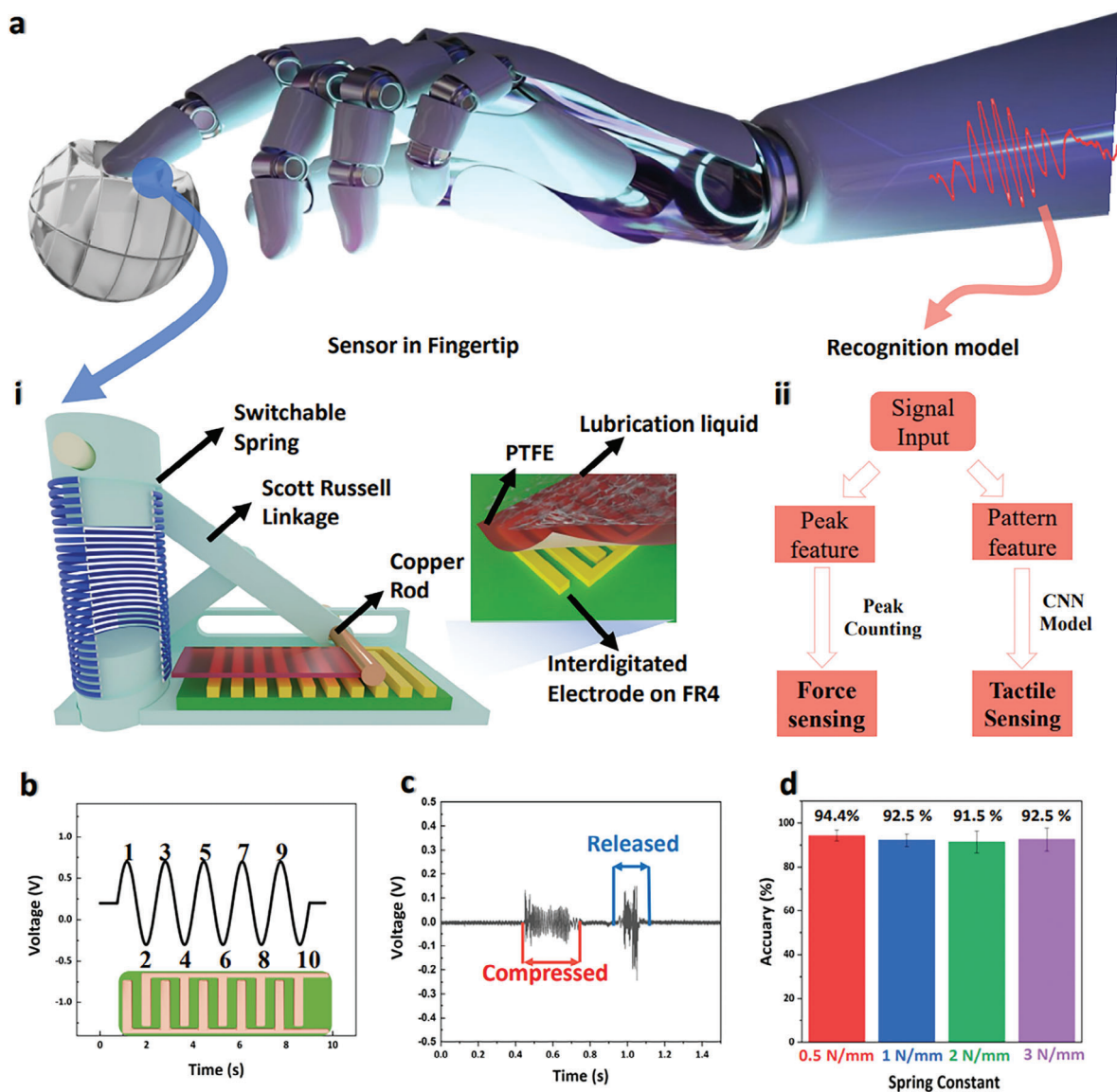
1. Introduction

The capability of Internet of Things (IoT), consisting of broad sensor networks, is rapidly growing in convergence with artificial intelligence (AI). Among the various types of sensors in the IoT area, the force sensor is widely used for smart manufacturing, health monitoring, and robotics.[1–4] As force is one of the core concepts in physics, force sensors can provide intuitive information about the physical phenomena that occur in 3D space through contact. However, conventional force sensors rely on external power sources such as batteries, which leads to maintenance challenges, increased costs, environmental waste, and various operational difficulties. To overcome these challenges, recent studies have focused on the development of self-powered sensors based on photovoltaic,[5–7] piezoelectric,[8–10] and radio frequency (RF).[11,12] Among these sensors, the triboelectric nanogenerator (TENG) is an energy harvesting technology suitable for not only driving functional electric components,[13–15] but also self-powered sensors owing to its simple structure,[16] material selection diversity,[17] and low fabrication cost.[18] TENG can convert mechanical movements into electrical signals based on a combination of contact electrification and electrostatic induction.[19,20] Therefore, TENG-based force sensors use external mechanical motion as input to generate electrical signals on their own.[21–23] In conventional TENG-based force sensors, the magnitude of the peak voltage is used to measure the external force.[24–26] However, the surface charge of the triboelectric material governs the magnitude of the TENG output signal, the magnitude of the peak voltage is material-dependent, because the external surface of the contacting material directly makes contact with the TENG.[27–29] This phenomenon negatively affects the accuracy and reliability of the readings of the sensor. In addition, because TENG-based sensors are generally fabricated using polymers and inevitably experience friction, their lifespans are limited because of frictional wear. Therefore, the development of a robust self-powered TENG force sensor that considers both external electrical influences and mechanical lifespan is required.

In this study, we demonstrate a Scott–Russell linkage-inspired TENG (SRI-TENG) that can be used as a self-powered force sensor. The Scott–Russell linkage in the SRI-TENG converts vertical displacement into horizontal displacement using the translation joint in the horizontal axis. When a vertical external force is applied, the horizontal movement through the Scott–Russell linkage can generate high-frequency AC electrical signals through a freestanding-type TENG. Unlike conventional TENG-based force

D. Seo, J. Kong, J. Chung
School of Mechanical System Engineering
Kumoh National Institute of Technology
61, Daehak-ro, Gumi-si, Gyeongsangbuk-do 39177, Republic of Korea
E-mail: jihoon@kumoh.ac.kr

**ADVANCED
SCIENCE NEWS**

www.advancedsciencenews.com

**NANO · MICRO
small**

www.small-journal.com

Figure 1. Scott–Russel linkage inspired triboelectric nanogenerator (SRI-TENG). a) Schematic illustration of SRI-TENG. (i) Structure of SRI-TENG, and (ii) signal processing model b) Open-circuit voltage (V_{OC}) passing over the electrode. c) V_{OC} output of the SRI-TENG when the force is applied and released. d) Dependence of accuracy on various spring constants of the SRI-TENG.

sensors, which utilize the magnitude of the generated peak voltage, the SRI-TENG can measure the contact force based on the number of electrical peaks generated. The number of peaks is governed by the compressed length of a spring. This enables precise force measurements that are independent of the surface charge of the contacting surface. Because the vertical movement of the switchable spring in the SRI-TENG is dependent on the spring constant, the dynamic range of the SRI-TENG can be adjusted by simply using an appropriate spring in its application. In the wide dynamic range, the SRI-TENG measured precise average sensing accuracy as 92.7%. In addition, a lubricant applied to the top layer of the TENG can prevent wear and guarantee a longer lifespan. Even after 225 000 operation cycles, the SRI-TENG generated a similar electrical output without a decrease in the amplitude or number of peaks. Furthermore, the possibility

of utilizing the SRI-TENG as a tactile sensor was demonstrated by applying a deep-learning model. SRI-TENG exhibited a 92% accuracy in classifying five objects with different tactilities. The SRI-TENG developed in this study can function independently of the contact surface of the external material, making it versatile for recognizing tactile and external forces in state-of-the-art technologies.

2. Result and Discussion

Figure 1a shows a schematic of the SRI-TENG system. To recognize the tactile force and measure the applied force, contact is inevitable. However, direct contact between the material and the TENG surface is necessary to determine the tactile force and measure the applied force. However, this contact affects the

ADVANCED
SCIENCE NEWS

www.advancedsciencenews.com

NANO · MICRO

small

www.small-journal.com

electric signal output because the TENG output is heavily governed by the triboelectric series between the two contacting surfaces. To prevent the contact surface charge from affecting the electrical output, the SRI-TENG system (Figure 1a-i) is designed using the following components: a Scott–Russell linkage, switchable spring, lubrication liquid on the PTFE film, and an interdigitated electrode (IDE). When the external surface makes contact with the measuring point, which is on the upper side of the Scott–Russell linkage, the spring connected to the measuring point is compressed. The vertical movement of the spring is converted into a horizontal movement through the Scott–Russell linkage, and the copper rod on top of the freestanding TENG can move depending on the vertical motion. As the contacting surface is separated from TENG, which generates the electrical signal, the output is unaffected by the surface charge of the material.

As shown in Figure 1a-ii, the signal can be analyzed using two methods. For force sensing, the peak feature is utilized. The SRI-TENG system generates multiple electrical peaks when an external force is applied. Considering the IDE dimensions and the initial position of the copper rod, the displacement of the compressed spring can be used to measure the applied force. For tactile recognition, features of output patterns can be used, which varies depending on the rigidity of the material. However, directly using features of the output pattern from TENG can be difficult due to external influences or unwanted triboelectric effects.[30] There is a need for an effective method to classify these output patterns. Among many existing classification deep learning algorithms for time series data, 1D convolution neural network (1D-CNN) is used. 1D-CNN performs only 1D convolutions and extracts features by itself. Although 1D-CNN requires a large dataset, sometimes can consume more time for training and needs a proper labeling process compared to other algorithms,[31,32] the 1D-CNN model excels in powerful feature extraction for time series data. 1D-CNN has a simpler structure, requires no dimensional changes for time series data, is efficient in test time, and has achieved high performance in many sensing application areas.[33–36] Given that the output of SRI-TENG is time series data, this advantage of 1D-CNN allows SRI-TENG to effectively recognize the tactile properties of a material.

Figure 1b and Figure S1 (Supporting Information) show the correlation between the electrical output generated by the SRI-TENG and the IDE arrangement. When horizontal movement occurs, the copper rod on top of the SRI-TENG slides over the freestanding-type TENG, which consists of a PTFE and an IDE on top of the FR-4 substrate. This generates a high-frequency frequency AC electrical signal. Initially, the difference in the triboelectric series results in copper becoming positively charged and PTFE negatively charged (Figure S1-i, Supporting Information). As the copper rod shifts to the right, the electrical equilibrium between the PTFE and right-side electrode breaks. The electrons from the electrode on the left side flow to the right side to equalize the potential difference (Figure S1-ii, Supporting Information). When the copper rod moves completely to the right-side electrode, the surfaces of the copper rod and PTFE form a new electrical equilibrium state (Figure S1-iii, Supporting Information). In addition, when the copper rod starts to move the electrode on the left side, electrons flow in the opposite direction, creating an opposite electrical current (Figure S1-iv, Supporting Information). As the copper rod moves between the two electrodes, the

electrons move back and forth to the left and right electrodes of the TENG, resulting in an AC sinusoidal output. As shown in Figure 1b, the number of peaks generated by the SRI-TENG represents the number of IDE. By counting the number of peaks generated, the displacement of the copper bar is measured and utilized to calculate the external force applied to the sensor.

Figure 1c shows the overall open-circuit voltage (V_{OC}) output of the SRI-TENG when an external force is applied. The kinematic movement of the Scott–Russell linkage can be defined by the conversion of the vertical spring movement to a horizontal movement in the SRI-TENG system. When an external force is applied, the spring is compressed and generates an AC electrical signal, depending on the number of IDE arrays. After the external force is removed, the compressed spring is released, and the copper rod moves back to its original position and generates a signal. Overall, two sets of electrical outputs can be observed when an external force is applied to and removed from the SRI-TENG.

Furthermore, Figure 1d shows the accuracy of the expanded dynamic range. The springs inside the SRI-TENG system can be switched to different spring constants spring. This indicates that the dynamic range of the sensor varies depending on its application. As shown in the figure, SRI-TENG shows high accuracies of 94.4%, 92.5%, 91.5%, and 92.5% when 0.5, 1, 2, and 3 N mm^{-1} springs are used, respectively.

Figure 2a is a simplified illustration of the SRI-TENG. The origin of the coordinates is point O, and the linkage moves along the x- and y-axes. The initial positions of the links are represented by Y_0 and X_0. When the y-axis linkage moves from point Y_0 to point O with a displacement of Y_B during compression, the x-axis linkage shifts from point X_0 to point A with displacement X_A. As shown in the illustration, the length of each linkage (AC, BC, and OC) is the same as L, and triangle OAB is a right triangle. Based on geometry, and assuming that linkages AB and OC are rigid bodies, the following equation can be obtained:

$$Y_0^2 + X_0^2 = (2L)^2 \tag{1}$$

When point A shifts according to the constraint conditions, the positions of points A and B are obtained using the following equations:

$$\begin{aligned} X_{A0} &= X_O + X_A \\ Y_{B0} &= Y_O - Y_B \end{aligned} \tag{2}$$

As the mass on the x-axis moves toward point A, the y-axis moves vertically toward point B. The relationship compared to the initial condition can be written as
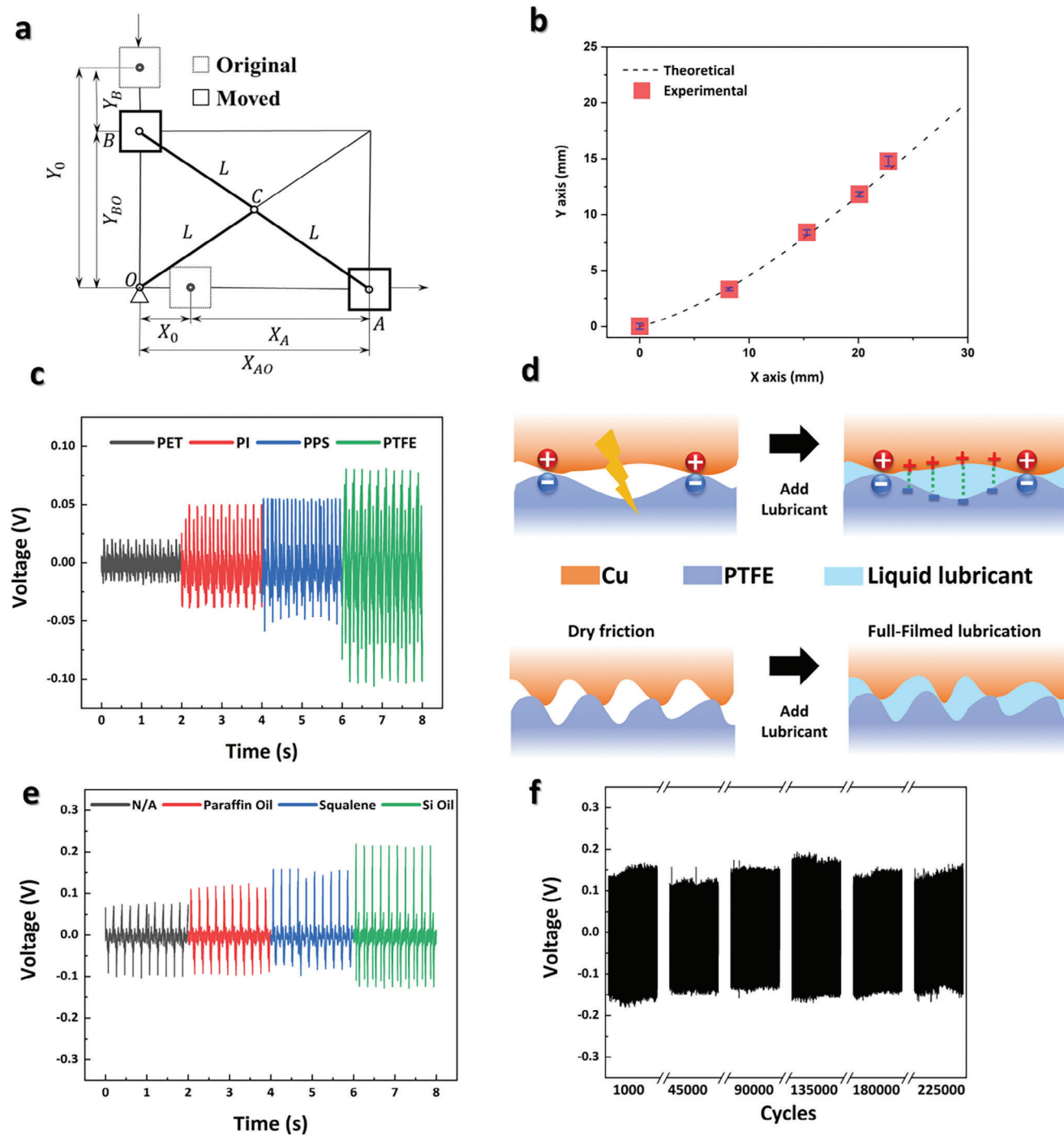
$$Y_0^2 + X_0^2 = (X_0 + X_A)^2 + (Y_O - Y_B)^2 \tag{3}$$

By simplifying Equation (3), it can be rewritten as

$$Y_B^2 - 2Y_O Y_B + 2X_O X_A + X_A^2 = 0 \tag{4}$$

By solving Equation (4) for Y_B, we obtain the following equation:

$$Y_B = -Y_O \pm \sqrt{Y_O^2 - 2X_O X_A - X_A^2} \tag{5}$$

Figure 2. Mechanism of force sensing and sensor performance feature. a) Kinematic model of the Scott–Russell mechanism. b) Displacement of the Scott–Russell mechanism between the theoretical model and experiment measurement. c) V_{OC} output depends on different triboelectric materials. d) Microscale schematic of copper and PTFE surfaces at contact when lubricant is applied on the SRI-TENG. e) Enhanced V_{OC} output depending on different types of lubricant. f) Durability results of SRI-TENG for 225000 cycles.

Considering the geometric relationship, the final displacement equation of point B can be written as

$$Y_B = -Y_O + \sqrt{Y_O^2 - 2X_O X_A - X_A^2} \qquad (6)$$

Therefore, by substituting the measured x-axis displacement (X_A) into Equation (6), we can obtain Y_B. Y_B represents the compressed distance of the spring, which indicates that the sensor can measure the applied external force by dividing it by the spring constant. A plot of the theoretical displacement versus the

**ADVANCED
SCIENCE NEWS**

www.advancedsciencenews.com

**NANO · MICRO
small**

www.small-journal.com

experimentally measured displacement is shown in Figure 2b. The initial conditions are $Y_0 = 39.5$ mm and $X_0 = 10$ mm. The experimental data fit the theoretical model. This indicates that the SRI-TENG system can precisely measure displacement.

Figure 2c shows the V_{OC} output according to the triboelectrification-layer materials used in the SRI-TENG. Owing to its triboelectric series and surface charges,[37] polytetrafluoroethylene (PTFE) shows the highest voltage output compared to PET, PI, and PPS. Because the number of peaks is used to measure the distance moved by the copper rod, a high signal-to-noise ratio (SNR) is required, considering the precision of peak counting and signal processing. Therefore, PTFE, which exhibits the highest V_{OC} peak value is selected as the triboelectrification layer in the SRI-TENG system to attain a high SNR.

Figure 2d shows the output enhancement and friction reduction mechanisms achieved by introducing a liquid lubricant. During the dry-friction process, the triboelectric charge on the surface is exposed to air; it is lost by air breakdown when the electrical potential difference reaches the breakdown voltage.[38] To suppress breakdown, a liquid lubricant is added between the surfaces of the two materials and the gap is submerged in the liquid. Because the breakdown voltage of the liquid lubricant is higher than that of air, it can suppress the loss of triboelectric charge on the surface[39–41] (Figure 2d-i). In addition, numerous contact points form on the asperity tips of the surfaces at the microscopic level. This leads to high contact pressure and subsequent plastic deformation when the two materials slide (Figure 2d-ii). This deformation causes cold welding and the formation of strong adhesive bonds between the two materials in contact. Strongly bonded cold welds must be sheared for sliding.[42] This phenomenon contributes to surface damage and negatively affects the lifespan of the sensor. However, under full-film lubrication conditions, the asperity tips are submerged, and this allows the liquids to support the entire external force. This suppresses cold welding, thereby improving the durability of the device surface.[43] Commercial lubricant liquids are tested to determine their ability to suppress surface discharge, enhance the negative charge on the PTFE surface, and avoid surface damage.

Figure 2e shows the V_{OC} output when various liquid lubricants are applied to the SRI-TENG. The peak voltages of paraffin, squalene, and silicone liquid are 0.12, 0.15, and 0.21 V, respectively. Unlike in dry conditions, with a liquid lubricant, the overall output of the SRI-TENG is higher. When a lubricant is applied to a triboelectric surface, the electric double layer (EDL) is a major factor that influences electrical output.[44] When a charged solid and a liquid make contact, the liquid forms an EDL, and the thickness of the EDL can be defined as the Debye length (λ_D).[45] For lengths within the Debye length, the electrostatic potential of a solid surface is not screened; however, it is screened for lengths beyond the Debye length.[46] Thus, a large Debye length ensures that a wider surface area is affected by the triboelectric charge. Thus, a lubricating liquid that can produce a long Debye length can generate a higher electrical output.

Figure 2f shows the V_{OC} output for a sensor operating at a 1 Hz input for 72 h (225 000 cycles). As shown in the plot, the SRI-TENG system continues to generate a similar electrical output even after 225 000 cycles, maintaining the initial output. This demonstrates that the lubricating oil can protect the surface from

damage by supporting an external force and that the SRI-TENG system can be utilized for robust external force measurement.

Furthermore, the electrical output of the SRI-TENG system was analyzed under various spring constants, dynamic ranges, and contact surface material conditions. **Figure 3a** shows a V_{OC} output of the SRI-TENG system and the number of peaks for springs with spring constants ranging from 0.5 and 3 N mm^{-1} under an external force of 4.9 N. As shown in the plot, the SRI-TENG with a spring whose spring constant is 3 N mm^{-1} generates 15 peaks, while with a spring constant of 0.5 N mm^{-1} shows 54 peaks, which is ≈3.6 times more. When a spring with a high spring constant (3 N mm^{-1}) is used, the length of the spring compressed is shorter compared to the SRI-TENG with a lower spring constant (0.5 N mm^{-1}). This indicates that the x-axis displacement of the SRI-TENG (X_A in Figure 2a) with a high spring constant is smaller and consequently generates fewer peaks. In contrast, X_A is much longer when a low-spring-constant spring is used, resulting in the generation of more peaks.

Figure 3b. shows the number of peaks from the V_{OC} output plot at an applied force of 4.9 N under for springs with spring constants ranging from 0.5 to 3 N mm^{-1}. The corresponding V_{OC} output plot for each spring constant is provided in Figure S2 (Supporting Information). When springs with spring constants of 0.5, 1, 2, and 3 N mm^{-1} are utilized, the average number of peaks is 56, 36.25, 20.25, and 14.25, respectively. As shown in the plot, the number of peaks gradually decreases as the spring constantly increases. This indicates that the sensitivity and dynamic range of the SRI-TENG system can be easily adjusted depending on the application, by simply replacing the spring component with springs having different spring constants.

Figure 3c shows the dynamic range of the SRI-TENG system with different spring constants. The spring components used in the SRI-TENG have spring constants of 0.5 (above), 1, 2, and 3 N mm^{-1} (below). As shown in the plot, the number of peaks can be used to calculate X_A using the dimensions of the IDE array. The compression spring length can be obtained using Equation (6), and the external force applied to the SRI-TENG can be measured using the following equation:

$$F = kx_{\text{TENG}} \tag{7}$$

where k is the spring constant, and x_{TENG} is the x-axis displacement. When a spring with a constant (0.5 N mm^{-1}) is inserted into the SRI-TENG system, the measured forces are 82, 198.5, 309.8, 417.3, 550.3, 632.1, 716.3, and 792.7 g, respectively, from the applied input force in the range of 100–800 g. For the spring with a spring constant of 1 N mm^{-1}, applying forces in the range from 300 to 600 g in 200 g intervals, the corresponding measured forces are 285.5, 377.7, 447.5, and 538.9 g, respectively. Furthermore, in the 2 N mm^{-1} spring constant condition, the SRI-TENG system generates forces of 538.8, 767.2, 895.1, and 1087.8 g, under the application of external forces 600 to 1200 g in 200 g intervals. In addition, when the applied force is 1000, 1200, 1500, and 2000 g the measured force is 856.5, 1110.9, 1427.6, and 2062.8 g respectively. This indicates that the SRI-TENG system can be used to accurately measure forces over a broad dynamic range by simply switching its spring constant.

Figure 3d and Figure S3 (Supporting Information) illustrate the number of peaks and V_{OC} output depending on the

ADVANCED
SCIENCE NEWS
www.advancedsciencenews.com

NANO · MICRO
small
www.small-journal.com
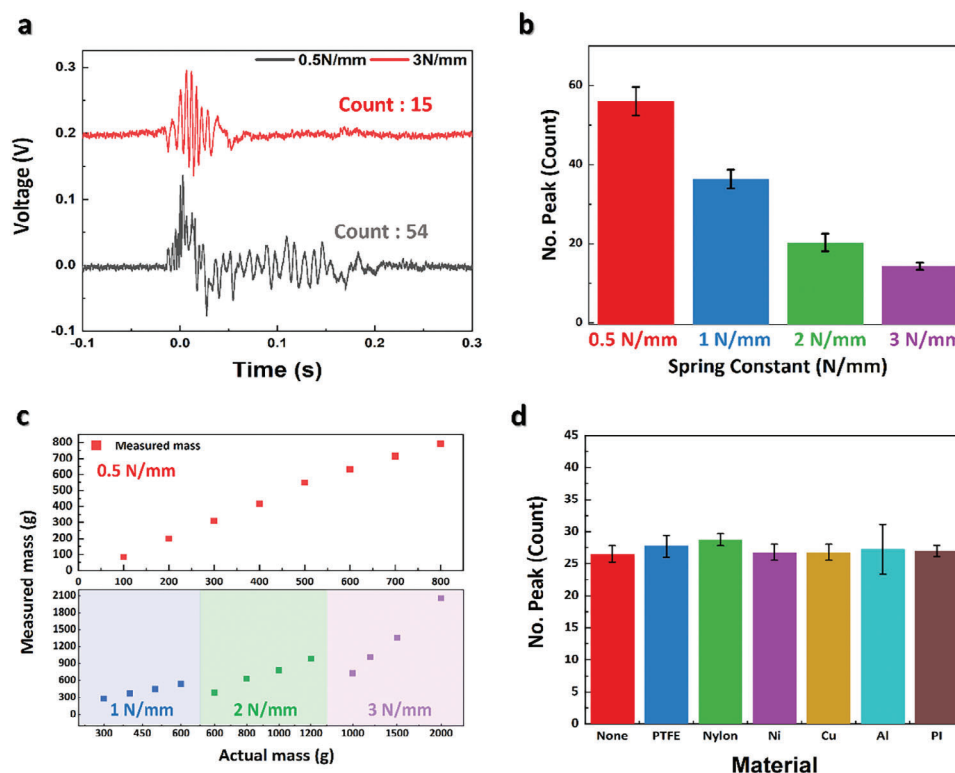
Figure 3. Performance of SRI-TENG. a) VOC and b) the number of peaks under different spring constants. c) The dynamic range of SRI-TENG with different spring constants. d) A number of peaks depends on various counterpart materials.

following contact surface materials: PTFE, nylon, nickel, copper, aluminum, and polyimide. The materials are attached to the weight surface, and the signal output is measured under the same weight conditions. These materials have different surface charges,[47] which affect the V_{OC} output of the SRI-TENG system if the contacting surface is in direct contact with the TENG. The VOC output of conventional TENG depending on the contacting material is shown in Figure S4 (Supporting Information). As shown in the graph, the electrical output varies depending on the contacting material. The electrical output of the SRI-TENG system is made independent of the contacting surfaces by converting the external force to a horizontal movement through the Scott-Russell linkage. As shown in the plot, PTFE and PI, which have negatively charged surfaces, have an average number of peaks of 27.75 and 27 peaks, respectively. In addition, nylon, nickel, aluminum, and copper, which have relatively positively charged surfaces, generated 28.75, 26.75, 27.25, and 26.75 average number of peaks, respectively. Representative materials with negative and positive surface charges exhibit similar numbers of peaks. This indicates that the SRI-TENG system generates an output that is unaffected by the material of the contacting surface. Therefore, the number of generated peaks is only force-dependent, regardless of the composition of the contact surface. The characteristics of the SRI-TENG system enable its use in various force-measuring situations with accurate force measurements.

As the electrical output of the SRI-TENG system is independent of the contacting surface, the SRI-TENG system can generate accurate signals from external forces regardless of the con-

tacting surface material. The generated signal can contain information regarding the applied force as the number of peaks and secondary information on the surface tactile data, which is shown as a pattern of the generated peaks. However, the pattern of the tactile information is unclear, and the data cannot be directly converted into force measurements. Machine learning is one of the best solutions for subtle signal feature extraction when an SRI-TENG system is used as a multimodal sensor.

Figure 4a shows a schematic of the operation of the SRI-TENG system, from signal acquisition to tactile recognition. In the initial step, the SRI-TENG generates a signal from an external contact. The signal is measured and converted into digital data. Subsequently, the data preprocessing process is performed on the signal from the previous step. A fast Fourier filter is utilized for external noise filtering in the measurement device, dimension reduction is applied to reduce the training time, and data normalization and preprocessing are used for high classification accuracy. Considering the characteristics of the signal generated signal by the SRI-TENG system, the timing of signal generation is important. This indicates that the order of the data is more important than the information of the surrounding data. The 1D-CNN algorithm is applied for data recognition because of its appropriateness for timeseries data and fast response.[48] Consequently, using a trained deep-learning model, the SRI-TENG system can distinguish the tactile information of the contacting surface. To utilize the 1D-CNN method in the SRI-TENG system and train the deep-learning model, materials with five different rigidities are fabricated, as described in the following experimental section. Each material is attached to a 500 g weight surface, and the

ADVANCED
SCIENCE NEWS

www.advancedsciencenews.com

NANO · MICRO

small

www.small-journal.com
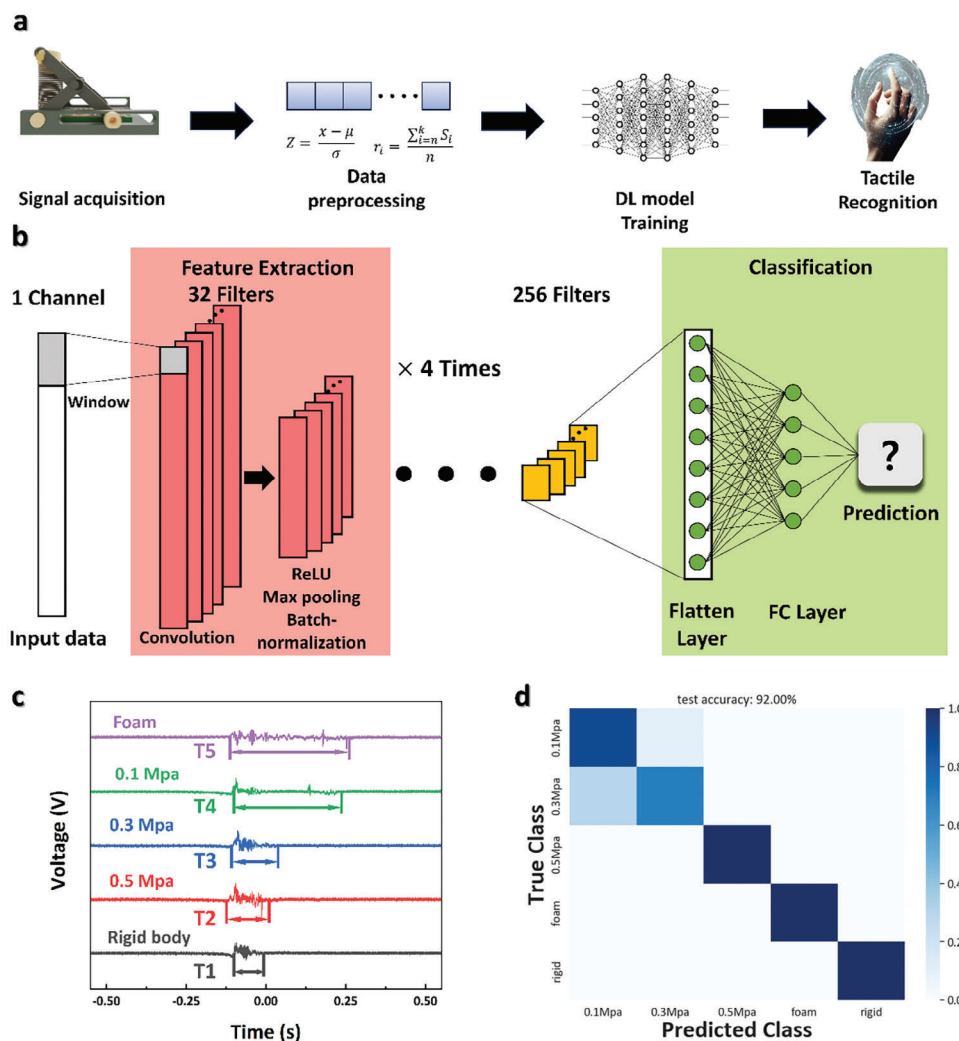
Figure 4. Tactile recognition of SRI-TENG. a) Schematic of data processing and recognition. b) Structure of the tactile recognition model. c) V_{OC} output in different rigidity of counter material. d) Confusion matrix of the tactile recognition.

multimodal signal is recorded from the SRI-TENG system when the surface makes contact with the measuring point and the spring is fully compressed. The total dataset contains 250 samples, and each class contains 50 data samples. From each class, 60%, 20%, and 20% of the 50 samples are randomly split into the train data set, validation data set, and testing data set, respectively. After splitting the dataset, the CNN model is trained using 50 training iterations.

Figure 4b illustrates the 1D-CNN structure. The 1D-CNN model consists of four convolution layers, four max-pooling layers, and fully connected layers. The detailed parameters are listed in Table S1 (Supporting Information). The convolution and pooling layers analyze the preprocessed signals and extract the features. The fully connected layer classifies the classes based on features extracted from the multimodal signal.

Figure 4c shows the responses of the SRI-TENG system for materials with Young's Moduli of 0.1, 0.3, and 0.5 MPa, and a rigid body. If the applied force does not depend on time and the contact force is equivalent, time is the only variant that can

change the generated signal. Under these conditions, the rigidity of the material can be explained by Young's modulus. When the Young's modulus is high, less time is required for deformation; conversely, when the Young's modulus is low, more time is required for deformation. The response signal shows that a harder material generates longer signals. This indicates that the SRI-TENG system recognizes tactile signals. The duration differences between 0.3, 0.5 MPa, and the rigid body signal are evident, but the 1D-CNN model is utilized to distinguish ambiguous signals by extracting unclear data such as the signals from 0.1 MPa foam.

As shown in Figure 4d, the trained CNN model exhibits a high recognition accuracy of 92% for the test data set of five different materials. The validation and training losses are presented in Figure S5 (Supporting Information). As the epochs progress, the training and verification accuracies converge to 1. Moreover, the verification and training losses converge to zero. While the training loss is maintained at zero, the verification loss remains at zero and does not diverge to a high loss. This indicates that the trained

model is not an overfitting model. Consequently, the SRI-TENG system successfully recognized tactile stimuli with high accuracy and without overfitting and can be used universally.

3. Conclusion

In summary, a material-independent triboelectric force sensor whose dynamic range can be modified by switching its spring was developed. The Scott–Russell linkage mechanism was studied based on a geometric relationship, and a theoretical model was suggested. The theoretical model accurately fits the actual motion of the SRI-TENG, indicating that the model can explain the displacement of the SRI-TENG system. Furthermore, by introducing a lubricant liquid, the SRI-TENG system can enhance both output and mechanical durability. The V_{OC} output increased by more than three times compared with dry conditions, and the system exhibited excellent output durability over 72 h (225 000 cycles). The force measurement characteristics of the SRI-TENG were investigated under various dynamic ranges and for different contact surfaces. Under these conditions, a relationship between the number of peaks and applied force was observed for the SRI-TENG. In addition, contact material recognition using 1D-CNN was demonstrated. SRI-TENG has shown a high accuracy of 92% without external power sources. This is attributed to a simple linkage structure of SRI-TENG, which effectively isolates the measurement and the signal-generation components. By integrating a self-powered TENG sensor based on Scott-Rusell linkage and robust data processing algorithms, we enhanced the accuracy and reliability of the sensor data. Our experimental results and comparative analysis show the potential of this approach for contact material-independent tactile recognition and external force detection.

4. Experimental Section

Fabrication of a Scott–Russell Structure-Inspired TENG (SRI-TENG): The SRI-TENG consists of a Scott–Russell linkage and TENG components. A polylactic acid filament (DY AIR) and a 3D printer (Flash Forge Adventurer3 Lite) were used to fabricate the Scott–Russell linkage components. The parts were printed at a 70 mm s^{-1} printing speed, and the temperature of the plate was 85 °C. Once all the parts had been printed, they were assembled. The TENG was fabricated using a printed circuit board (PCB). The width and length of the PCB were 12.7 and 32 mm, respectively, and the substrate thickness was 1.6 mm. The PCB contained a total of 98 electrodes, and the gap and thickness of the electrodes were 150 µm, as shown in Figure S6 (Supporting Information). A 50 µm-thick PTFE film was attached on the upper side of the PCB electrodes as a triboelectric layer, and then the PCB was attached to the Scott–Russell linkage as shown in Figure S7 (Supporting Information).

SRI-TENG Spring Constant Adjustment Procedure: The SRI-TENG can switch its spring constant for appropriate measurements. Any spring can be mounted when the spring meets the standard. The procedure is shown in Figure S8 (Supporting Information).

Fabricating tactile samples: Polyurethane (PU) foam, ecoflex-30 (Smooth-On), and Sylgard184 (Dupont) were used to fabricate the different tactile samples. The area of the material, which had a cylindrical shape, was ≈12.5 cm^2 and the height was 1.5 cm. The fabrication method for samples with different Young's modulus has been previously reported.[49] Each silicone sample was mixed according to the manufacturer's recommendations. For Sylgard184, the ratio was 10:1(Part A:Part B, wt%), and for Ecoflex, it was 1:1(Part A:Part B). After pre-mixing, different silicones

Table 1. Mixing ratio and properties of different silicone elastomer mixtures.

No.	Young's modulus	Part A	Ratio	Part B	Ratio
1	0.1 MPa	Sylgard 184	-	EcoFlex	1
2	0.3 MPa	Sylgard 184	1	EcoFlex	3
3	0.5 MPa	Sylgard 184	3	EcoFlex	1

were obtained according to the mixing ratios shown in **Table 1**. Each mixture was placed in a vacuum chamber for 5 min to degas then cast into a mold and dried in an oven under 80 °C for 2 h. Different tactile materials were obtained by peeling the dried silicone from the mold. The foam was cut into the same shape as the sample, and all samples were attached to a weight.

Measurement: The open-circle voltage signal of the SRI-TENG was measured using a digital oscilloscope (Tektronix MDO34). Mechanical input is given during the durability experiment with a function generator (AFG3021C, Tektronix Co.), vibration tester (ET-126B-4, Labworks Co.), and preamplifier (pa-151, Labworks Co.).

Supporting Information

Supporting Information is available from the Wiley Online Library or from the author.

Conflict of Interest

The authors declare no conflict of interest.

Author Contributions

D.S. performed conceptualization, methodology, validation, formal analysis, investigation, visualization, wrote the original draft, and reviewed and edited the final manuscript. J.K. performed methodology and investigation. J.C. performed conceptualization, methodology, validation, supervision, visualization, and reviewed and edited the final manuscript.

Data Availability Statement

The data that support the findings of this study are available from the corresponding author upon reasonable request.

ADVANCED
SCIENCE NEWS

www.advancedsciencenews.com

NANO · MICRO
small

www.small-journal.com

[1] S. Matuska, M. Paralic, R. Hudec, *Mob. Inf. Sys.* **2020**, *2020*, 1.

[2] Z. Bi, Y. Liu, J. Krider, J. Buckland, A. Whiteman, D. Beachy, J. Smith, *J Ind Inf Integr* **2018**, *11*, 19.

[3] C. Chuang, D. Lee, W. Chang, W. Weng, M. O. Shaikh, C. Huang, *IEEE Sens. J.* **2017**, *17*, 2498.

[4] Z. Kappassov, J. Corrales, V. Perdereau, *Rob. Auton. Syst.* **2015**, *74*, 195.

[5] H. Michaels, M. Rinderle, I. Benesperi, R. Freitag, A. Gagliardi, M. Freitag, *Chem. Sci.* **2023**, *14*, 5350.

[6] M. K. Mishu, M. D. Rokonuzzaman, J. Pasupuleti, M. Shakeri, K. S. Rahman, S. Binzaid, S. K. Tiong, N. Amin, *Sensors.* **2021**, *21*, 2604.

[7] M. D. Rokonuzzaman, M. K. Mishu, N. Amin, M. Nadarajah, R. B. Roy, K. S. Rahman, A. M. Buhari, S. Binzaid, M. Shakeri, J. Pasupuleti, *Micromachines.* **2021**, *12*, 653.

[8] X. Cao, Y. Q. Xiong, J. Sun, X. Zhu, Q. Sun, Z. L. Wang, *Adv Funct Mater.* **2021**, *31*, 2102983.

[9] M. Shirvanimoghaddam, K. Shirvanimoghaddam, M. M. Abolhasani, M. Farhangi, V. Zahiri Barsari, H. Liu, M. Dohler, M. Naebe, *IEEE Access* **2019**, *7*, 94533.

[10] G. Hu, Z. Yi, L. Lu, Y. Huang, Y. Zhai, J. Liu, B. Yang, *Nano Energy* **2021**, *87*, 06140.

[11] M. B. Lam, N. T. Dang, T. Nguyen, W. Chung, *IEEE Sens. J.* **2019**, *19*, 8813.

[12] L. Cui, Z. Zhang, N. Gao, Z. Meng, Z. Li, *Sensors* **2019**, *19*, 4012.

[13] Y. Ra, Y. Kim, S. Yang, N. Kang, G. Oh, C. Cho, S. Lee, D. Choi, *Nano Energy* **2023**, *119*, 109052.

[14] S. Zhou, S. Liao, K. Sun, Z. Zhang, Y. Qian, P. Liu, P. Du, J. Jiang, Z. Lv, S. Qi, *Laser Photonics Rev.* **2023**, *18*, 2300464.

[15] B. Fan, X. Zhao, J. Zhang, Y. Sun, H. Yang, L. J. Guo, S. Zhou, *Laser Photonics Rev.* **2023**, *17*, 2200455.

[16] D. Kim, K. Cha, H. Ryu, M. Song, S. Kim, Z. Lin, J. Chung, S. Lee, *Adv. Eng. Mater.* **2023**, *25*, 2201760.

[17] R. Zhang, H. Olin, *EcoMat.* **2020**, *2*, 12062.

[18] Y. Li, Z. Zhao, Y. Gao, S. Li, L. Zhou, J. Wang, Z. L. Wang, *ACS Appl Mater Interfaces* **2021**, *13*, 30776.

[19] W. Kim, D. Kim, I. Tcho, J. Kim, M. Kim, Y. Choi, *ACS Nano* **2021**, *15*, 258.

[20] S. Wang, L. Lin, Y. Xie, Q. Jing, S. Niu, Z. L. Wang, *Nano Lett.* **2013**, *13*, 2226.

[21] J. Son, D. Heo, Y. Song, J. Chung, B. Kim, W. Nam, P. T. J. Hwang, D. Kim, B. Koo, J. Hong, S. Lee, *Nano Energy* **2021**, *93*, 106797.

[22] K. Xia, C. Du, Z. Zhu, R. Wang, H. Zhang, Z. Xu, *Appl. Mater. Today* **2018**, *13*, 352.

[23] J. Syamini, A. Chandran, *ACS Appl. Electron. Mater.* **2023**, *5*, 1002.

[24] A. K. K. Aminullah, J. K. Kasi, M. Uddin, M. Bokhari, *Curr. Appl. Phys.* **2019**, *20*, 137.

[25] X. Shang, N. Wang, S. Cao, H. Chen, D. Fan, N. Zhou, M. Qiu, *Adv. Mater.* **2023**, *36*, 2305121.

[26] B. Shan, C. Liu, R. Chen, G. Qu, H. Sui, N. Chen, G. Xing, *Mater. Today Nano* **2023**, *24*, 100391.

[27] J. Huang, S. Wang, X. Zhao, W. Zhang, Z. Chen, R. Liu, P. Li, H. Li, C. Gui, *Mater. Horiz.* **2023**, *10*, 3840.

[28] S. Mu, S. Li, H. Zhao, Z. Wang, X. Xiao, X. Xiao, Z. Lin, Z. Song, H. Tang, Q. Xu, D. Wang, W. W. Lee, C. Wu, W. Ding, *Nano Energy* **2023**, *116*, 108790.

[29] T. Li, J. Zou, F. Xing, M. Zhang, X. Cao, N. Wang, Z. L. Wang, *ACS Nano* **2017**, *11*, 3950.

[30] R. Li, D. Wei, Z. Wang, *Nanomaterials* **2024**, *14*, 165.

[31] S. Kiranyaz, O. Avci, O. Abdeljaber, T. Ince, M. Gabbouj, D. J. Inman, *Mech Syst Signal Process* **2020**, *151*, 107398.

[32] Y. Chen, Z. Lin, X. Zhao, G. Wang, Y. Gu, *IEEE J. Sel. Top. Appl. Earth Observations Remote Sensing* **2014**, *7*, 2094.

[33] I. Mitiche, A. Nesbitt, S. Conner, P. Boreham, G. Morison, *IET Generation, Transmission & Distribution.* **2020**, *14*, 5766.

[34] J. Yu, Y. Wen, L. Yang, Z. Zhao, Y. Guo, X. Guo, *Nano Energy* **2021**, *92*, 106698.

[35] A. Kamilaris, F. X. Prenafeta-Boldú, *J Agric Sci* **2018**, *156*, 312.

[36] D. Li, J. Zhang, Q. Zhang, X. Wei, *2017 IEEE 19th International Conference on e-Health Networking, Applications and Services (Healthcom)*, IEEE, New York City, **2017**, p. 1.

[37] E. Shin, J. Ko, H. Lyeo, Y. Kim, *Phys. Rev. Research.* **2022**, *4*, 23131.

[38] Z. Xu, J. Duan, W. Li, N. Wu, Y. Pan, S. Lin, J. Li, F. Yuan, S. Chen, L. Huang, B. Hu, J. Zhou, *ACS Appl Mater Interfaces* **2019**, *11*, 3984.

[39] W. He, W. Liu, S. Fu, H. Wu, C. Shan, Z. Wang, Y. Xi, X. Wang, H. Guo, H. Liu, C. Hu, *Research* **2024**, *2022*, 9812865.

[40] J. Chung, S. Chung, Z. Lin, Y. Jin, J. Hong, S. Lee, *Nano Energy* **2021**, *88*, 106292.

[41] L. Zhou, D. Liu, Z. Zhao, S. Li, Y. Liu, L. Liu, Y. L. Gao, Z. L. Wang, J. Wang, *Adv. Energy Mater.* **2020**, *10*, 02002920.

[42] D. Arnell in *Mechanisms and laws of friction and wear*, Elsevier, Amsterdam **2010**, pp. 41–72.

[43] L. C. Duque-Ossa, G. Ruiz-Pulido, D. I. Medina, *Polymers* **2021**, *13*, 746.

[44] L. Zhong, Z. L. Wang, *Adv. Energy Mater.* **2020**, *10*, 2001770.

[45] S. Chung, J. Chung, M. Song, S. D. Kim, D. Shin, Z. Lin, B. Koo, D. Kim, J. Hong, S. Lee, *Adv. Energy Mater.* **2021**, *11*, 2100936.

[46] W. Huang, A. K. Diallo, J. L. Dailey, K. Besar, H. E. Katz, *J Mater Chem* **2015**, *3*, 6445.

[47] H. Zou, Y. Zhang, L. Guo, P. Wang, X. He, G. Dai, H. Zheng, C. Chen, A. C. Wang, C. Xu, *Nat. Commun.* **2019**, *10*, 1427.

[48] S. M. Shahid, S. Ko, S. Kwon, *2022 International Conference on Information Networking (ICOIN)*, IEEE, New York City, **2022**, p. 507.

[49] J. Vaicekauskaite, P. Mazurek, S. Vudayagiri, A. L. Skov, *J Mater Chem* **2019**, *8*, 1273.

2403394 (9 of 9)